Chemical Engineering Journal 426 (2021) 130892

Contents lists available at ScienceDirect

Chemical Engineering Journal

journal homepage: www.elsevier.com/locate/cej

# High energy Na-Ion capacitor employing graphitic carbon fibers from waste rubber with diglyme-based electrolyte

Madhusoodhanan Lathika Divya [a,1], Sundaramurthy Jayaraman [b,1], Yun-Sung Lee [c], Vanchiappan Aravindan [a,*]

[a] Department of Chemistry, Indian Institute of Science Education and Research (IISER) Tirupati 517507, India
[b] Environmental and Water Technology Center of Innovation, Ngee Ann Polytechnic, 599489 Singapore
[c] School of Chemical Engineering, Chonnam National University, Gwang-ju, 61186, Republic of Korea

ARTICLE INFO

*Keywords:*
Na–ion capacitor
Graphitic carbon nanofibers
Solvent-co−intercalation
Low–temperature performance

ABSTRACT

Co–intercalation process using glyme-based solvents has brought new prospects for the reversible Na-intercalation into the graphitic materials. We report a high-energy Na-ion capacitor (SIC) with graphitic carbon nanofibers (GCNF) as a battery-type component obtained from the depolymerization of waste rubber. The kinetic study reveals that ~ 51% contribution is originated from the diffusion-controlled Faradaic mechanism for GCNF compared to the ~ 61% for commercial graphite powder. The synthesis procedure and less crystalline nature of the GCNF lead to the lowered intercalation potential, and extended Na-ion storage capacity in the lower potential region (*vs.* $Na^+/Na$) which is significant compared to the graphite powder. Further, the half-cell delivered a discharge capacity of ~ 118 mAh $g^{-1}$ irrespective of the applied current rate, which signifies the importance of this concept. In a SIC configuration with activated carbon, the SIC renders an energy density of 55.58 Wh $kg^{-1}$ at 25 °C. In addition, exceptional low-temperature performance (<10 °C) is noted with a maximum energy density of 54.69 Wh $kg^{-1}$ and > 97% capacity retention after 5000 cycles. This low-temperature performance, high energy density, and exceptional cyclability certainly offer a unique hybrid charge storage system that eventually explores the possibility of using graphitic carbon fibers towards balanced energy and power capabilities. On a lighter note, this study also provides the opportunity to handle the waste materials effectively for sustained charge storage applications.

## 1. Introduction

Achieving a net carbon–neutral economy is a real challenge, and it needs cost-effective energy storage systems[1]. At present Li-ion batteries (LIBs) represent the state-of-the-art energy storage device for all computers, smartphones, and electric vehicles (EVs). A drastic increase in Lithium demand due to usage in EV batteries brought a severe problem with its availability and price, which made the researchers find out substitutes to traditional LIBs. Sodium (Na)-ion batteries (NIBs) represent a decent green choice to consider as the next-generation energy storage solution mainly due to cost-effectiveness and abundance [2]. A metal-ion capacitor, MICs/hybrid capacitors (Li-ion capacitor, LIC), is another type of device on the market that combines high energy battery (LIB) and high-power supercapacitor (electric double-layer capacitor, EDLC) technology to the best of both. Sodium-ion capacitors (SICs) have also gained much attention due to the same reasons, like rich Na-sources and comparable performance to LICs. LIBs/SIBs store energy by electrochemical method and EDLCs hold energy by electrostatic charge storage mechanism. However, a MIC (LIC/SIC) contains one electrochemical or battery electrode and one electrostatic electrode[3-6]. Carbonaceous materials, conversion oxides, alloying metals, and titanium-based compounds have the potential to play the role of the negative electrode material in MICs[7]. However, carbon-based intercalation materials are preferred over other materials, as those materials suffered large irreversibility, huge volume variation, and poor cyclability[8-11]. Generally, dual-carbon MICs hold activated carbon (AC) positive electrodes and a metal-doped carbon-based material as the negative electrode combined with a liquid electrolyte[6,12-14]. To attain a notable performance in these MICs, both the electrodes ought to have greater charge storage capability and fast kinetics as the

* Corresponding author.
*E-mail address:* aravind_van@yahoo.com (V. Aravindan).
[1] Contributed equally.

https://doi.org/10.1016/j.cej.2021.130892
Received 3 May 2021; Received in revised form 31 May 2021; Accepted 14 June 2021
Available online 17 June 2021
1385-8947/© 2021 Elsevier B.V. All rights reserved.

electrode materials play a vital role in determining the device's performance. Generally, the battery type negative electrode materials exhibit sluggish metal-ion diffusion kinetics, resulting in hybrid capacitors with poor rate performance[15-17]. Moreover, in comparison with Li counterparts, many issues affect Na-based reactions' irreversibility and remain unsolved. Hence, further research is very much essential to find out the suitable Na-intercalating materials.

Graphite is one of the most successful intercalation-based negative electrode for LIBs because of its high specific capacity with low intercalation potential and productivity[18]. During Li intercalation, graphite forms a series of binary graphite intercalation compounds (*b*-GICs) with a final composition of $LiC_6$. However, the graphite was considered an inappropriate material for Na-based systems due to the thermodynamic instability of *b*-GICs with intercalated Na-ions[19]. Recently, the research groups of Jache *et al.*[20] and Kim *et al.*[21] investigated Na-ion intercalation into graphite using the phenomenon of co-intercalation/solvated Na-ion intercalation with linear ether solvents, and that leads to the formation of ternary GICs (*t*-GICs). It was also reported that the co-intercalation could be fast, comparable to the conventional Li-ion intercalation process. Moreover, the co-intercalation voltage differs with the nature of the solvent used, and the phenomenon is intrinsically different from conventional metal-ion intercalation due to the complex interaction between solvent and guest molecule. Recently, we have reported on the fabrication of graphite-based SICs with the co-intercalation mechanism[22] and several other groups for SIB perspectives[23]. Thus, the glyme-based solvents created novel chances for graphitized materials in Na-based systems assembly with fascinating electrochemical insertion mechanism[24-26].

The transformation of plastic and other industrial waste materials into carbonaceous material for a charge-storage application is a sustainable approach in handling huge waste and offers a new path for the fabrication of affordable energy storage devices according to the "trash-to-treasure" approach. Recently, carbon nanofibers (CNF) have gained much consideration as active electrode material in both batteries and supercapacitor applications[27-34]. Their unique morphology and small diameter favours fast charge–discharge in the electrochemical device assembly. The atomic structure of carbon fiber is analogous to graphite, in which flat sheets of carbon atoms (graphene layers) are organized in a regular hexagonal pattern. These 1D materials exhibit different properties like shorter diffusion pathways and a high surface-to-volume ratio. Based on the precursor type, the carbon layers can be either turbostatic, graphitic, or hybrid form[7]. The utilization of graphitic carbon nanofibers (GCNF) as negative electrode for Li-based systems and as supercapacitor electrodes have been previously reported with conventional carbonate-based electrolytes[35-37]. In this study, we report the synthesis of GCNF using depolymerized oil obtained by pyrolysis of waste rubbers as precursor material. Rubber products have turn out to be a mainstay in all our endeavours today. Moreover, nearly 279 million tires get discarded every year and eventually become a significant potential waste and cause environmental problems[38-40]. These factors led to the necessity to develop suitable methods to reuse this waste material. We report co-intercalation-based SIC assembly, using pre-sodiated GCNF as the battery type negative electrode and AC as the counter electrode with diglyme-based electrolyte. The capacitive contribution in the electrochemical charge storage for the GCNF electrode is measured and compared with that of a commercial graphite electrode under the same electrolyte. Besides, the performance of assembled SIC at different temperature conditions were also studied

## 2. Experimental section

### 2.1. Synthesis of graphitic carbon nanofibers (GCNF)

Depolymerized oil obtained by pyrolysis of waste rubbers was collected from the local supplier and used as the carbon feed source. Stainless steel (SS) plate was employed as a catalyst. The graphitized fibers were synthesized by a modified catalytic chemical vapor deposition (CVD) process. Firstly, the catalyst was pre-cleaned in diluted nitric acid solution to remove the surface impurities and create surface roughness on the catalyst. Then the catalyst was placed in a cleaned quartz tubular furnace for the CVD process. The oil was placed in a separate closed container. A thermocouple, coupled with an external heater, was employed to maintain the constant temperature of 250 °C in the closed container until the completion of the CVD process. The inert nitrogen gas of 120 ml $min^{-1}$ flow rate was passed through the heated oil. The depolymerized low carbon chain molecules from the heated oil were collected by the inert nitrogen gas and supplied as a carbon feed source to the quartz furnace. Pure nitrogen was initially purged to remove air from the furnace. The furnace was maintained at a pressure of around 760 torr and a temperature of 800 °C for 5 h. The hydrogen gas was passed along with the carbon feed nitrogen gas in the ratio of 1:4 to 1:6 after the furnace reached the set temperature. The unreacted gas was passed through the de-ionized water before venting out. The graphitized fibers were scrapped from the catalyst and directly used for the electrochemical studies.

### 2.2. Characterizations

The powder X-ray diffraction pattern of graphitized fibers was recorded by X-ray diffractometer (XRD, Rigaku, Smartlab 9 kW, Japan) with Cu Kα radiation. Raman spectrum of the sample was obtained by Raman spectroscopy (LabRam HR800 UV Raman microscope, Horiba Jobin- Yvon, France). The surface elemental composition was examined with X-ray photoelectron spectroscopy (XPS with a Multilab instrument (monochromatic Al Kα radiation $h\nu = 1486.6$ eV). The surface morphology and the material's core structure were analyzed with a field emission scanning electron microscope (FE-SEM, S-4700, Hitachi, Japan) and a High-resolution transmission electron microscope (HR-TEM, HR-TEM, TECNAI, Philips, the Netherlands, 200 keV). The elemental analysis of GCNFs was performed in the STEM nanoprobe mode with high angle annular dark-field imaging (HAADF) detector.

### 2.3. Cell assembly and electrochemical measurements

The GCNF working electrodes were prepared by a slurry coating method using a doctor blade. In a typical process, GCNFs are mixed with conductive carbon (acetylene black) and binder (polyvinylidene fluoride, PVdF) in the ratio 80:10:10 using N-methyl pyrrolidone (NMP) solvent; and was kept under constant stirring overnight to ensure the formation of a homogeneous slurry. Then it was coated on Cu-foil with a doctor's blade apparatus, and the coated foil was dried out in a hot air oven and then pressed under a hot roll press (Tester Sangyo, Japan). Disc electrodes of 14 mm diameter were punched out with the help of an electrode cutter. Activated carbon (AC, YP-80F, Kuraray, Japan) was used as the active electrode material for the counter electrode (positive electrode). Electrode fabrication was done with the help of mortar and pestle by mixing the active material (AC, 80%) with 10% conductive carbon (acetylene black) and 10% binder (teflonized acetylene black, TAB-2) using ethanol solvent. A thin layer of electrode material was pressed on a 14 mm diameter SS-mesh current collector (Goodfellow, UK). Before the cell assembly, both the electrodes were dried under a vacuum chamber at 75 °C for a minimum period of 4 h. The half-cells and SIC fabrication were done in the form of coin-cell assembly (CR 2016) under the Ar-filled glove box using 0.5 M $NaPF_6$ salt (98%, Sigma-Aldrich) in diethylene glycol dimethyl ether (DEGDME) electrolyte and Whatman paper (1825–047, GF/F) as a separator. For the GCNF and AC half-cell assembly, Na metal foil was used as the counter and reference electrodes. For SIC fabrication, initially, pre-sodiation of GCNF electrode was done in half-cell assembly, and further, the cell was dismantled, and the GCNF electrode in discharged condition was paired with AC electrode of balanced mass. Battery tester BCS 805 (Biologic, France) was

used for testing the electrochemical performance of both Na/GCNF and Na/AC half cells and SICs. Electrochemical Impedance Spectroscopy (EIS, at an applied a.c. amplitude of 10 mV in the range of 10 kHz to 1 Hz), cyclic voltammetry (CV), and galvanostatic charge–discharge studies were carried out to analyze the assembled coin-cells. Also, the fabricated hybrid SIC device's performance at different temperature conditions was tested with the help of an environmental chamber (Espec, Japan).

## 3. Results and Discussion:

### 3.1. Graphitic carbon nanofibers (GCNF)

The GCNFs were synthesized by modified chemical vapor deposition using waste rubber-derived depolymerized oil as the precursor. A high degree of graphitization is ideal for electrochemical applications, as it reduces internal resistance and enhances the power performance of the device[41]. The structure and degree of graphitization of as-synthesized material were analyzed by both X-ray diffraction (XRD) (Fig. 1(a)) and Raman spectra (Fig. 1(b)). The reflection around 26.4° in the XRD pattern is ascribable to the (002) peak of graphite (JCPDS card number 75–1621) with an interplanar spacing of 3.37 Å[42]. Using the classical Scherrer equation over (002) peak with a geometrical factor (K) value of 0.9, the crystallite size was 11.20 nm. The reflection around 45° can be allocated to the convolution of (100) and (101) peaks, which corresponds to reflections of carbon nanocrystallines [43]. When comparing with the XRD pattern of commercial graphite (Sigma-Aldrich), Figure S1, (002) peak of GCNFs is broader than that of graphite. The broad and low-intensity peak indicates the formation of nanostructured material with less crystallinity in comparison with commercial-grade graphite. Comparing the area under the peak (002) of both the samples, the quality of crystalline state of GCNFs is analyzed and found to be ~ 2.6 times less than that of the graphite sample. Raman spectrum of the material showed three prominent peaks at ~ 1345, ~1572, and ~ and 2697 $cm^{-1}$, which corresponding to D, G, and 2D bands, respectively. The D band is assigned to a disordered band, or defects band originates from hybridized vibrational mode linked with graphene edges and indicates structural defects, whereas G band, graphite, or tangential band arises from stretching of C − C bond in graphitic material[44]. The intensity ratio between the D and G band ($I_D/I_G$) represents the degree of graphitization and is obtained as ~ 0.61, which corresponds to a high degree of graphitization. The 2D band initiates from two phonon double resonance processes, and it is indicative of the degree and type of graphene layer stacking. The intensity ratio of 2D and D band ($I_{2D}/I_D$ = ~0.74) is indicative of the overall crystalline quality of the graphitic network, and it rises with long-range ordering, and the ratio of $I_G/I_{2D}$ (~2.29) is a clear indicator of the existence of multilayer graphene sample[45-48]. The absence of characteristic peaks/bands of any impurities in XRD and Raman spectroscopy defines the quality of the material synthesized.

The elemental composition of the material surface was analyzed by X-ray photoelectron spectroscopy (XPS), and the survey spectrum of GCNF, Figure S2 exhibits C1s and O1s peaks with the calculated At.% values of C1s (~94.54%) and O1s (~5.46%), indicating ~ 94.54% sample purity with a negligible degree of oxidation. In the high-resolution C1s spectra Fig. 1(c), the prominent peak at 284.6 eV is allocated to C–C bonds of $sp^2$ hybridized carbons and the other two peaks at 285.88 and 287.33 eV is assigned to C in C–OH and C = O bonds, respectively. The O1s spectra Fig. 1(d) is deconvoluted into three peaks with peak maxima of 532.34, 533.89, and 530.95 eV, which correspond to C − O, O–C = O, and C = O groups, respectively[49,50]. The obtained data is also consistent with the XRD and Raman spectroscopy result pointing to the high degree of graphitization of the material synthesized. Field emission-scanning electron microscope (FE-SEM) images, Fig. 2(a, b), and transmission electron microscope (TEM) images Fig. 2(c, d & e) disclosed the morphological features of one-dimensional elongated hollow carbon nanofibers with an average diameter of ~ 20–30 nm. The crystallinity of the material is observed from HR-TEM images, which show the presence of multi-layered graphene sheets. The elemental analysis of GCNFs was performed in a STEM

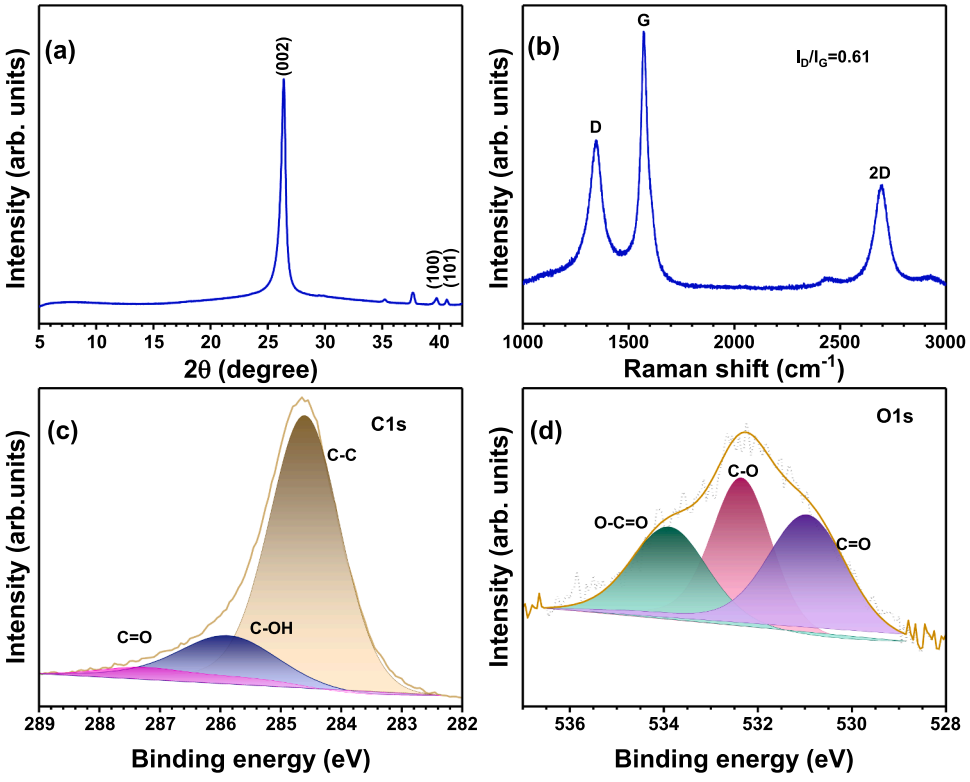


**Fig. 1.** Physical properties of GCNF: (a) XRD pattern, (b) Raman spectrum and XPS (c) C1s spectrum, (d) O1s spectrum of graphitic carbon nanofibers.

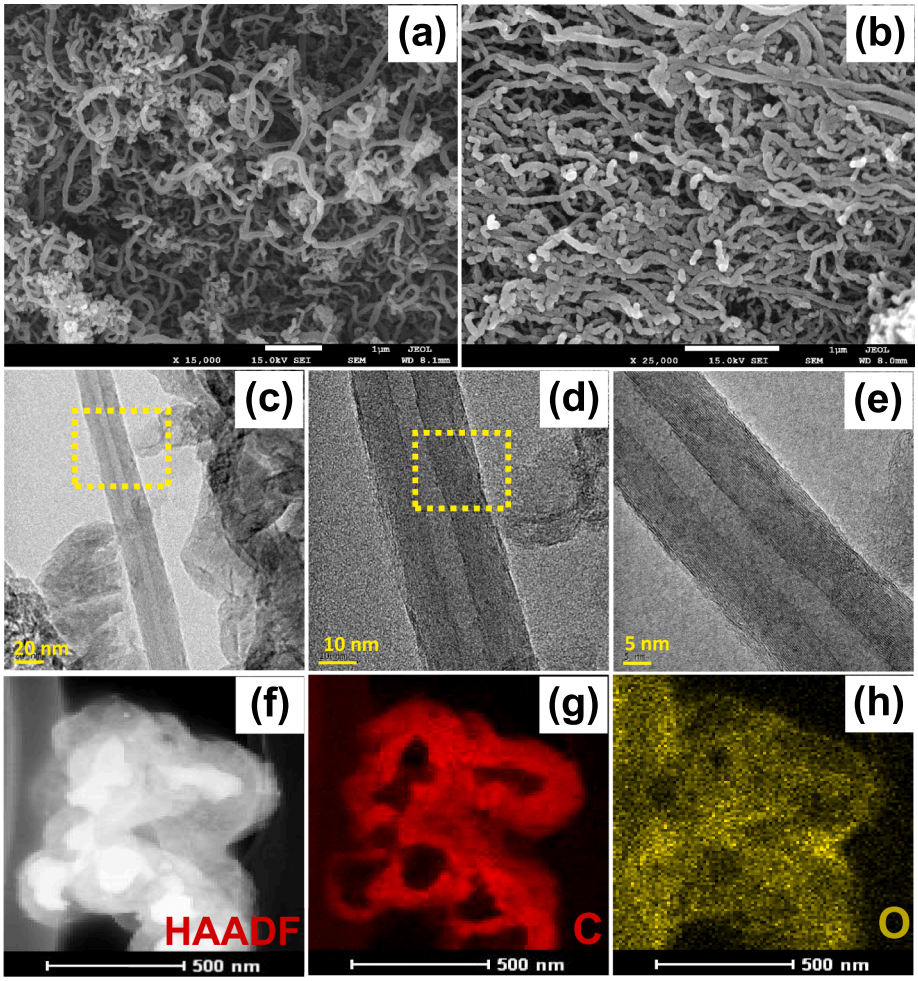


**Fig. 2.** Morphological features of GCNF: (a, b) FESEM image; (c, d, e) TEM image ; (f) HAADF – STEM image and selected area for elemental mapping using EDS; (g) mapped carbon; (h) mapped oxygen.

nanoprobe equipped with a HAADF detector. Fig. 2(f) illustrates the STEM/HAADF image of synthesized nanocrystalline material and the square-shaped area selected for the elemental analysis. The elemental mapping of C and O is clearly seen in Fig. 2(g) and Fig. 2(h), respectively. The BET surface area of the GCNF was calculated to be 19.72 $m^2$ $g^{-1}$ (Figure S3).

### 3.2. Electrochemical studies

To evaluate the performance of GCNFs as a battery-type electrode material (negative electrode) for co–intercalation-based SIC assembly, the negative electrode half-cells were fabricated with Na-metal as a reference and counter electrode in the presence of 0.5 M $NaPF_6$ in DEGDME solution as the electrolyte. After a rest period of 4 h, the fabricated half-cells displayed an open circuit voltage (OCV) of ~ 2 V *vs.* $Na^+$/Na, which corresponds to the equilibrium potential of the GCNF electrode as the potential of Na metal is always 0 V *vs.* $Na^+$/Na[51]. The electrochemical performance of the Na/GCNF half–cell configuration was analyzed with CV, galvanostatic charge–discharge (GCD), and EIS. Fig. 3(a) shows the CV profile of Na/GCNF half-cell at a scan rate of 0.1 mV $s^{-1}$. The current profile in the first discharge is different from the remaining cycles as the material is undergoing activation. The graphene layers in the GCNF have to be expanded for the first time[52,53]. This activation process can be seen in the form of a broadened reduction peak within the potential window of 0.6–0.0 V *vs.* $Na^+$/Na. It was also reported that the Na-insertion brings strain, swelling and finally breaks the carbon nanofibers; hence it creates new pathways for Na-diffusion[53]. Moreover, there is the formation of a surface layer (solid electrolyte interface, SEI) due to electrolyte decomposition. From the second cycle onwards, the first cathodic peak is observed at ~ 0.56 V *vs.* $Na^+$/Na, whereas the corresponding anodic peak is located at ~ 0.75 V *vs.* $Na^+$/Na. Besides, there is one small reduction peak at ~ 0.03 V *vs.* $Na^+$/Na and a small anodic peak at ~ 0.08 V *vs.* $Na^+$/Na representing multiple solvated Na-ion intercalation sites into GCNF [53]. Fig. 3(b) displays the CV profile at different scan rates of 0.1–1 mV $s^{-1}$. Apparently, there is a shift in the cathodic peaks towards the low potential region and anodic peaks towards the high potential region with the increase in scan rate. It is also observed that the peak current intensity for the two major peaks ($C_1$ & $A_1$) changes linearly with the square root of scan rate representing a diffusion-controlled mode of reaction (Fig. 3(c)). With the Randles-Sevcik equation, the apparent diffusion coefficient corresponding to the diffusion of solvated Na-ions into/out-of GCNF at the selected potentials was calculated as ~ $0.6 \times 10^{-8}$ and $2.4 \times 10^{-8}$ $cm^2$ $s^{-1}$, respectively, based on cathodic and anodic peak currents.

In CV experiments, the current response to the scan rate varies irrespective of the type of redox reaction, whether it is diffusion-controlled or not[54]. Moreover, in nanomaterials, as the critical dimensions of energy storage are reduced to the nanoscale, the available diffusion path length is restricted, and there is an enhancement of surface area available for the non-diffusion limited charge storage. By considering the above points, it is essential to quantify the contribution of diffusion-controlled and non-diffusion-controlled redox reactions in the overall charge storage mechanism of battery – type carbon nanomaterials. The non-diffusion limited charge storage mechanism is

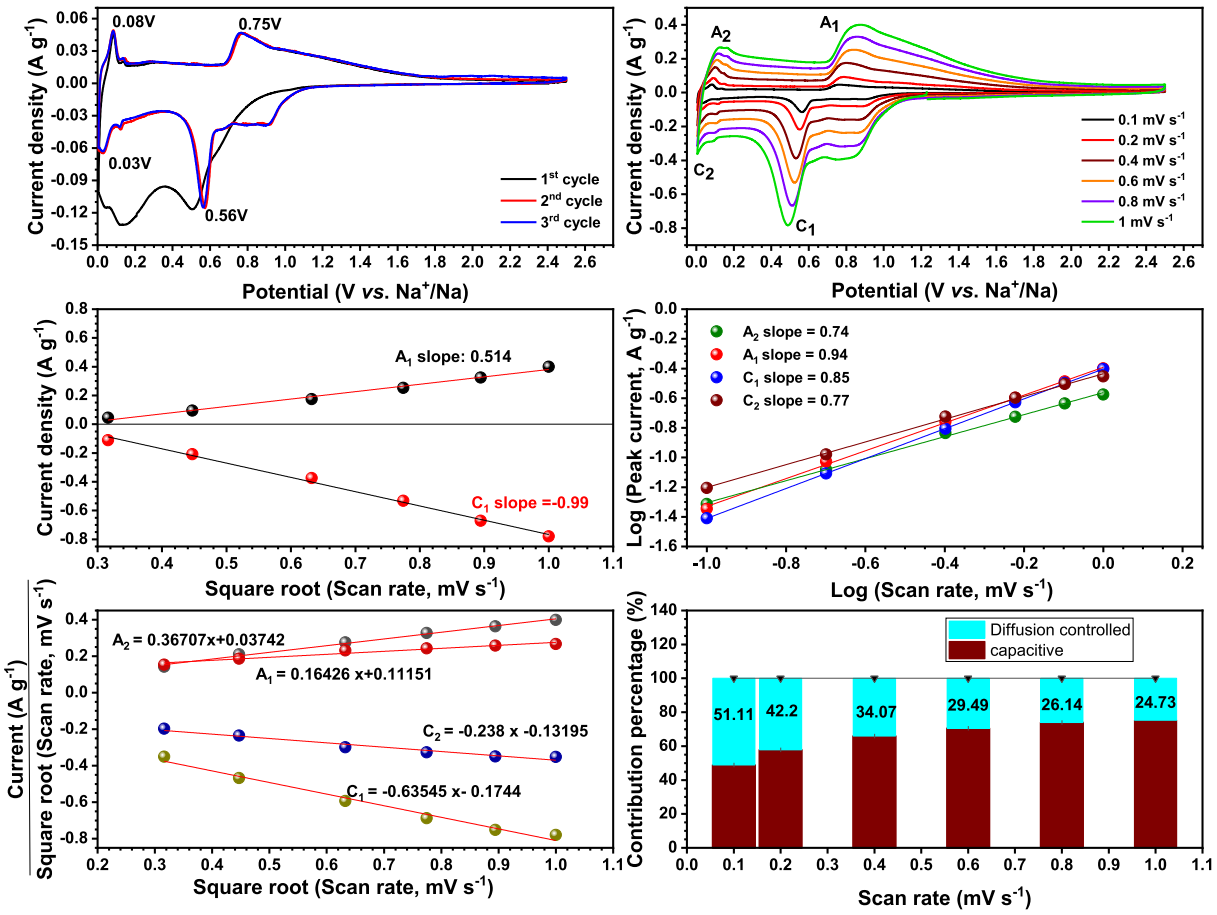


**Fig. 3.** Electrochemical kinetics analysis of Na/GCNF half - cell by Dunn method: a) CV profiles at a scan rate of 0.1 mV $s^{-1}$ for the first three cycles, b) CV profile at different scan rates, c) Linear plot of peak current ($i_p$) *vs.* square root of scan rate, d) Relationship between Logarithm scan rate and Logarithm redox peak currents (*b*-value determination), e) Plots of (scan rate) $^{1/2}$ *vs.* current (i). (scan rate) $^{-1/2}$ used to compute constants $k_1$ and $k_2$ at different potentials, and f) Percentage of diffusion-controlled and pseudocapacitive current at various scan rates.

known as capacitive or extrinsic pseudocapacitive charge storage. Kinetic analysis of GCNF material was performed according to the model proposed by Dunn *et al.*[55]. The power-law relationship between peak current ($i_p$) and scan rate ($\upsilon$) is studied by the equation $i_p = a\upsilon^b$, where $a$ and $b$ are adjustable parameters. The value of $b = 0.5$ represents a semi–infinite linear diffusion limited Faradaic reaction, while $b = 1$ indicates pseudocapacitive or surface redox reaction[56]. The slope of ln ($\upsilon$) *vs.* ln($i_p$) plots for the cathodic and anodic peaks gives the values of b, Fig. 3(d), and is found to be between 0.5 and 1 for all the peaks, indicating the combination of diffusion-controlled and pseudocapacitive charge-storage mechanism in GCNFs. Surprisingly, for the major peaks C1 and A1, the *b* values are found to be ~ 0.85 and ~ 0.94, suggesting that the pseudocapacitive surface redox reaction is dominated by diffusion-limited charge storage. For the peaks C2 and A2, the *b* values are calculated to be ~ 0.77 and ~ 0.74, indicating equal contribution from diffusion-controlled and non-diffusion-controlled charge-storage mechanisms. Additionally, the current measured by CV at a fixed potential is expressed by the equation, $i = k_1\upsilon + k_2\upsilon^{1/2}$, where $k_1\upsilon$ and $k_2\upsilon^{1/2}$ , representing the contribution from the pseudocapacitive process and the diffusion-controlled Faradaic process, respectively. Fig. 3(e) illustrates the graph plotted for the determination of $k_1$ and $k_2$. It is used to quantify the percentage contribution from pseudocapacitive, and the diffusion-limited charge storage mechanism in GCNFs for different scan rates (Fig. 3(f)). Thus, only ~ 51% of the total current at 0.1 mV $s^{-1}$ is contributed by a diffusion-controlled Faradaic charge storage mechanism. The pseudocapacitive contribution increases towards higher scan rates, indicating the dominance of surface redox reaction at a faster charge–discharge process. Furthermore, the performance is compared with that of commercial graphite samples in the same electrolyte system, Figure S4. It was observed that the percentage contribution from pseudocapacitive or surface redox reaction is more in the case of GCNFs (49% @0.1 mV $s^{-1}$) in comparison with commercial graphite sample (39% @0.1 mV $s^{-1}$) Figure S5. Although the difference between the Faradaic process is ~ 10%, however, there are two important observations worth mentioning for the case of GCNFs, (i) solvation intercalation process happens at the lower potential (~0.56 and ~ 0.60 V *vs.* $Na^+$/Na for the GCNF and graphite, respectively), and (ii) extended and reversible storage at lower potentials (reduction and oxidation potential of ~ 0.03 and ~ 0.08 V *vs.* $Na^+$/Na, respectively) compared to the commercial graphite. Such lower working potential is one of the most important pre-requisite to be imposed for the negative electrodes. Further, the solvation intercalation is one of the most complex processes, in which the extended storage close to the reference electrode (Na) certainly leads to realizing the high energy charge-storage devices when paired with the capacitor type electrodes irrespective of the mechanisms (*e.g.*, Faradaic or non-Faradaic component).

The potential *vs.* capacity curve of Na/GCNF half–cell recorded under the galvanostatic condition of 50 mA $g^{-1}$ is displayed in Fig. 4(a). The first discharge voltage curve exhibits a near-constant slope within the region between 0.6 and 0 V *vs.* $Na^+$/Na. In contrast, the voltage profile for the first charge and other subsequent cycles shows fluctuations in slope. The cell exhibits high irreversibility in the first cycle with an initial coulombic efficiency (ICE) of ~ 50%. This low ICE value indicates irreversible trapping of solvated $Na^+$ ions within the GCNF

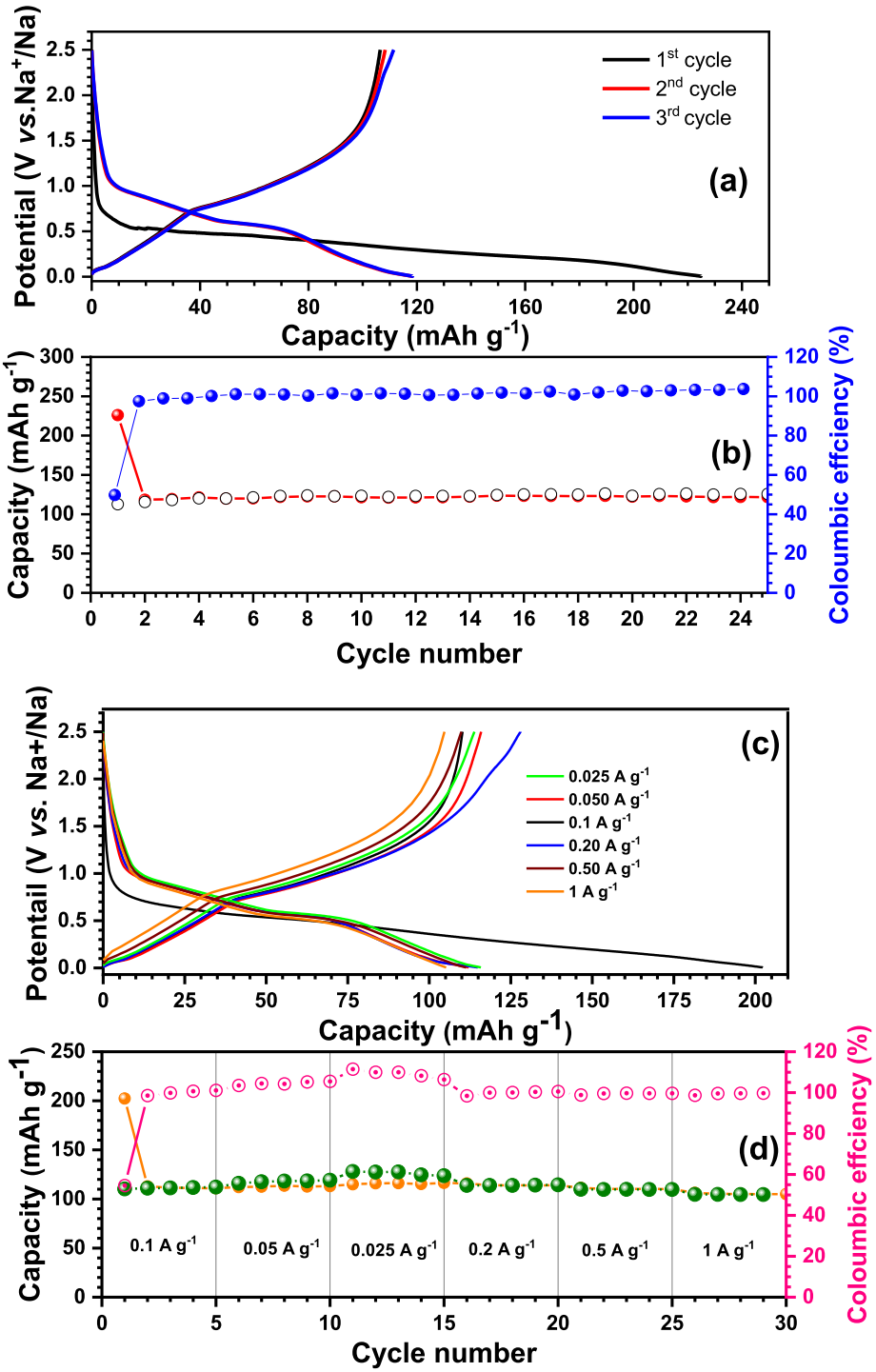


**Fig. 4.** Electrochemical performance of GCNF electrode in half-cell assembly with Na: a) Typical Charge -discharge profiles at 50 mA $g^{-1}$, b) Long-term cyclability at 50 mA $g^{-1}$, c) Performance at various current densities, and d) Cycling performance.

structure. At a current density of 50 mA $g^{-1}$, the assembled cells exhibit a maximum discharge capacity of ~ 118 mAh $g^{-1}$ within the potential window of 0.005–2.5 V *vs.* $Na^+$/Na. Regardless of irreversibility in the first few cycles, efficiency increased to > 99% (Fig. 4b), and Na/GCNF half-cells could maintain their capacity even after 100 cycles in Figure S6 (a &b). Fig. 4(c &d) represents the rate performance and cyclic stability of cells at various current densities. The cell could exhibit a discharge capacity of ~ 105 mAh $g^{-1}$ even at the high current rate of 1 A $g^{-1}$ with excellent reversibility. Further to examine the effect of Na-salt on solvated Na-ion storage behavior of GCNF, we conducted the galvanostatic charge–discharge study with 1 M $NaCF_3SO_3$ in DEGDME solution. However, an identical charge–discharge profile with a similar capacity was observed; Figure S6(c &d) indicates the nature of anion in the electrolyte which does not significantly affect the co-intercalation process. On the other hand, the type of solvent plays a major role in the cell's intercalation potential and rate capability, which we observed earlier for recovered graphite from spent LIB[22], and other groups also pointed that the salt has negligible influence in co-intercalation phenomena[57]. When the chain length and molecular weight of glyme increases, there is a rise in the cell's intercalation potential and drop-in

rate capability; for example, 0.5 M $NaPF_6$ in DEGDME solution is used as an electrolyte, and the low concentration can reduce the device's cost and expand the operating temperature range[58]. Moreover, due to the low solvation energy of Na-ions, fast transport, and the Na-based electrolytes are more conductive than Li-based solutions[59]. The excellent performance of GCNF encouraged us in exploring the possibility of using them in a practical device, for example, SIC with AC as a counter electrode.

Prior to the fabrication of the SIC, the mass loading between the electrodes are very crucial to attain a high energy density with durability. Generally, the mass loading between the electrodes is assessed based on the individual capacity of the electrodes with a common reference electrode (*vs.* $Na^+/Na$). In this line, the Na/AC half-cell is fabricated and tested at the same current density of 50 mA $g^{-1}$ within the potential window of 1.5– 4 V *vs.* Na. The Na/AC half-cells showed an OCV of ~ 3 V *vs*. $Na^+/Na$ in the presence of 0.5 M $NaPF_6$ in diglyme solution. The linear charge–discharge profile, Figure S7 (a), describes the surface adsorption/desorption process (non-Faradaic) with a discharge capacity of ~ 62 mAh $g^{-1}$. Therefore, the electric double layer (EDL) formed on the surface of the AC electrode accommodates oppositely charged ions at different potential ranges, which means adsorption of $PF_6^-$ ions from 3 to 4 V *vs.* $Na^+/Na$ and solvated Na-ions from 3 to 1.5 V *vs.* $Na^+/Na$ [6,60]. The cell exhibits > 95% capacity retention even after 200 charge–discharge cycles with high coloumbic efficiency (Figure S7 (b)). From the half–cell studies, it is clear that GCNF and AC electrodes can reversibly store solvated Na-ions with high stability, and hence it is used as the electrode materials for the fabrication of high-performance SIC.

### 3.3. SIC fabrication and performance analysis

SIC full-cells were fabricated using pre-sodiated GCNF and AC as negative and positive electrodes, respectively, in the presence of 0.5 M $NaPF_6$ in diglyme electrolyte. As mentioned, the charge balance between the two electrodes based on their specific capacities is essential to achieve optimum performance in hybrid capacitors as there is a sharp difference between the electrochemical kinetics of both the electrodes, Faradaic sodiation of solvated Na-ions in the battery type electrode, and non-Faradaic adsorption of solvated Na and $PF_6^-$ ions in the across the electrode electrolyte interface[6]. Thus, the SIC was assembled by maintaining a positive to negative mass ratio of ~ 1.5–2, which results in a total active material mass of ~ 17–19 mg in the device, with an active material mass of ~ 5–7 mg for the negative and ~ 11–12 mg for the positive electrode. The charge storage mechanism in the assembled SIC is an electrolyte-consuming process, in which, during charging, cations and anions present in the electrolyte are separated and moved to the negative and positive electrode under the action of voltage[61]. In the GCNF electrode, the solvated Na-ions are intercalated into the space between graphene layers, and for the AC electrode, $PF_6^-$ ions are subjected to physical adsorption[62]. During discharging, the solvated Na-ions are deintercalated from the GCNF electrode and go back to the electrolyte, whereas desorption of anions occurs at the AC electrode, which makes a charge balance to the system.

The electrode reactions can be represented by the equations,

Negative electrode: $GCNF + xNa[diglyme]_2^+ + xe^- \leftrightarrows GCNF\left[Na[diglyme]_2\right]_x$ ..... (1)

Positive electrode: $AC + PF_6^- \leftrightarrows AC^+PF_6^-(doublelayer) + e^-$ (2)

Equation (1) & (2) shows how the charge is stored in the negative electrode *via.* co-intercalation mechanism and how the charge is stored in the AC electrode *via.* charging of electrochemical double layer with $PF_6^-$ ions from the electrolyte. Pre-sodiation of the negative electrode is the process of doping a certain amount of $Na^+$-ions prior to the fabrication of a hybrid capacitor. The two prime objectives of pre-sodiation include (i) eliminating the effect of irreversible capacity in the first cycle, and (ii) adjusting the redox potential of the active material as close as that of $Na^+/Na$ to get a maximum working potential window [63]. The irreversible decomposition of electrolyte causes the extra capacity observed for the GCNF electrode in the first reduction step (maximum value is ~ 225 mAh $g^{-1}$), resulting in the formation of the SEI layer on the surface of the negative electrode or due to activation of GCNF electrode.

The electrochemical performance of the GCNF/AC-based SIC is illustrated in Fig. 5. The galvanostatic charge–discharge profile within the potential window of 1–3.5 V for different current rates measured at different temperature conditions is given in Fig. 5(a-d). The near-linear charge – discharge profile of the assembled SICs indicates the co–intercalation process's influence in the linear charge–discharge profile of AC. The distortions in the charge – discharge profile clearly show the involvement of two different charge storage mechanisms. As usual, an increase in current density tends to decrease charge–discharge time. Almost similar, a near triangular appearance without any major deviations represents the SIC's stability at different temperature conditions tested (-5,10, 25 & 50 °C). Fig. 5 (e) shows the Ragone plot, which gives the relationship between energy and power density of the assembled SIC. The specific values of energy and power density are calculated from the galvanostatic discharge curves by considering the total mass of active material present in both electrodes. The SIC could deliver a maximum energy density of 55.58 Wh $kg^{-1}$ at a power density of 133 W $kg^{-1}$ in the ambient temperature conditions. Even at a high-power density of 4.52 kW $kg^{-1}$, the device can deliver energy of 18.19 Wh $kg^{-1}$. Further, at high (50 °C) and low-temperature conditions (10 and − 5 °C), the SIC could display energy density values of 57.01, 54.69 & 49.78 Wh $kg^{-1}$, respectively. Apparently, the cell rendered almost similar performance at low power density irrespective of the temperature conditions imposed. However, there is a small drop in performance at higher rates with a fall in temperature. The cell's cyclability/durability is another very crucial factor to signify the potential impact for practical applications. The GCNF/AC-based SIC is subjected to the long-term cycling studies and given in Fig. 5 (f). At different temperature conditions, starting from –5, 10, 25 & 50 °C at a current density of 1 A $g^{-1}$, the assembled device could retain ~ 94, 97, 70 & 40% of initial capacity after 5000 charge–discharge cycles. It is very obvious to see the extremely stable performance of SIC, especially at low-temperature conditions (10 and − 5 °C). This study clearly suggests that the glyme-based SIC is a tailor-made device for low-temperature applications with high energy and durability. Even after 10,000 charge–discharge cycles at ambient conditions, the cell could retain ~ 45% of the initial capacity Figure S8 (a). If we impose the condition of 80% retention for practical use, the SIC can go up to ~ 3100 cycles at ambient temperature, whereas SIC can withstand only ~ 1850 cycles at 50 °C. Xu *et al.* [19] described that there is a negative shift in the electrode potential for co-intercalation with an increase in temperature. That can be assigned as the reason for low cyclic stability at high-temperature conditions. Interestingly, regardless of the temperature conditions, the SIC exhibits high reversibility, which is clearly seen from the coulombic efficiency (>99%). At room and elevated temperature conditions require some more attention for improvement under the solvation-intercalation concept.

As impedance spectra provided additional information about the kinetic response of electrode materials, Nyquist plots of fresh half – cells and assembled SIC are plotted and fitted with equivalent circuits generated by the Z fit technique, Figure S8 (b – d). They are mainly composed of an intercept of real axis, solution resistance (Rs) representing the resistance offered by electrode material and electrolyte, A semicircle in the middle to high frequency indicating the charge transfer resistance (Rc), and a sloping straight line in the low-frequency region, Warburg impedance W (in the case of Na/GCNF half –cell and SIC) corresponding to the diffusion of solvated Na-ions. The fabricated SIC's hybrid behavior was also confirmed by the CV profile recorded at a scan rate of 1 mV $s^{-1}$ in the voltage range of 1–3.5 V (Figure S9). The near rectangular shape of CV with small oxidation–reduction peaks also

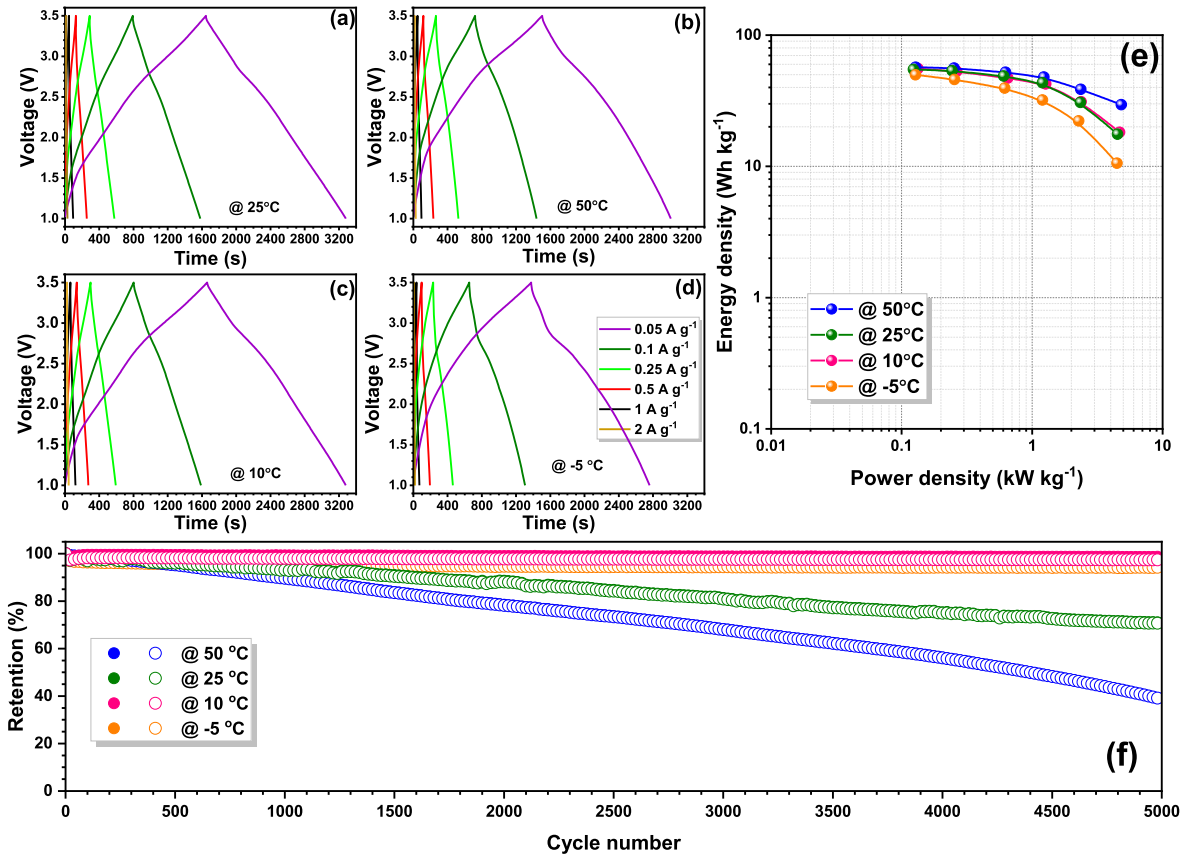


**Fig. 5.** Electrochemical performance of AC/GCNF based SIC cells: a, b, c &d) Typical galvanostatic charge–discharge profiles at different temperature conditions, e) Ragone plot describing Energy and Power density of the SIC at various temperature conditions, and f) Long term cyclability at the tested temperature conditions.

indicates the capacitive contribution of GCNF material at higher scan rates. Besides, we also examined the possibility of widening the voltage window of assembled SIC. Figure S10 illustrates the Ragone plot and GCD profile of SIC tested within the voltage window of 1–3.7 V. The as-fabricated device delivered a maximum energy density of 58.55 Wh $kg^{-1}$ at a power density of 117 W $kg^{-1}$ at ambient temperature conditions. Unfortunately, the cell experiences poor cyclability owing to the large surface area of both GCNF and YP 80F.

Therefore, we limited the working potential up to 3.5 V for the SIC and achieved superior electrochemical performance. Further, the fabricated SIC with waste rubber derived 1D graphitic carbon nanofiber negative electrode-based device performance can be compared with a recently reported co – intercalation mechanism using graphite as negative electrode material[22]. We could observe that the assembled device's energy density is almost matching with the graphite-based system, whereas the corresponding power density value is doubled [22]. This is fairly possible with the extended storage at the lower potential and reduced intercalation potential compared to the graphite. This study's findings confirm that graphitic carbon nanofibers (GCNFs) can be effectively used for the assembly of next-generation sodium-ion capacitors that undergo the solvation-intercalation process. Besides, the device's performance makes such systems suitable for considering as alternative energy storage systems where energy is not an ultimate parameter while power density, cycle life, and cost of the device are vital, particularly for low-temperature working conditions.

## 4. Conclusion

The 1D graphitized carbon nanofiber was used as a negative electrode for the fabrication of co–intercalation-based SIC with AC positive electrode under the optimized mass loading conditions. GCNFs have been successfully prepared by the CVD method using waste rubber-derived depolymerized oil as the precursor. The electrode kinetics, along with the solvated Na-ion storage property of the material, was evaluated in half – cell assembly. We observed that the capacitive contribution in the case of GCNF was more than the commercial graphite sample. The SIC working at 1–3.5 V could deliver a maximum energy density of 55.58 Wh $kg^{-1}$ at ambient temperature conditions with a capacity retention of 70% after 5000 charge–discharge cycles. This high energy and high power capability is mainly due to the lower intercalation potential and extended Na-storage at lower potentials, besides the appropriate optimization in the working potential and mass balance. The glyme-based SIC was tailor-made for the low-temperature conditions and required attention in the ambient and elevated temperature conditions in terms of the cyclability aspect. Nevertheless, this work is anticipated to promote the use of graphitized carbon nanofibers for the assembly of low-cost and efficient Na-based energy storage systems, moreover transforming the waste materials into functional carbon materials for the energy storage device as capable electrode materials is a supreme achievement in the scientific research.

## Declaration of Competing Interest

The authors declare that they have no known competing financial interests or personal relationships that could have appeared to influence the work reported in this paper.

## Acknowledgments

MLD wishes to thank the funding through Women Scientist Scheme-B (DST/WOS-B/2018/2039) from the KIRAN division of the Department of Science & Technology (DST), Govt. of India. YSL acknowledges the

financial support from the National Research Foundation of Korea (NRF) grant funded by the Korean government (Ministry of Science, ICT & Future Planning) (No. 2019R1A4A2001527). VA acknowledges financial support from the DST through Swarnajayanti Fellowship (DST/SJF/PSA-02/2019-20).

## Appendix A. Supplementary data

Supplementary data to this article can be found online at https://doi.org/10.1016/j.cej.2021.130892.

## References

[1] A. Colthorpe, Energy storage 'vital for carbon neutral Europe and Germany's Green Deal', 2 Jul 2020.
[2] K.M. Abraham, ACS Energy Lett. 5 (2020) 3544–3547.
[3] W. Zuo, R. Li, C. Zhou, Y. Li, J. Xia, J. Liu, Adv. Sci. 4 (2017) 1600539.
[4] A. Muzaffar, M.B. Ahamed, K. Deshmukh, J. Thirumalai, Renew. Sustain. Energy Rev. 101 (2019) 123–145.
[5] J. Ding, W. Hu, E. Paek, D. Mitlin, Chem. Rev. 118 (2018) 6457–6498.
[6] T. Panja, J. Ajuria, N. Díez, D. Bhattacharjya, E. Goikolea, D. Carriazo, Sci. Rep. 10 (2020) 10842.
[7] V. Aravindan, Y.-S. Lee, The Journal of Physical Chemistry Letters (2018) 3946–3958.
[8] E. Frackowiak, PCCP 9 (2007) 1774–1785.
[9] K. Zou, P. Cai, X. Cao, G. Zou, H. Hou, X. Ji, Curr. Opin. Electrochem. 21 (2020) 31–39.
[10] G. Li, Z. Yang, Z. Yin, H. Guo, Z. Wang, G. Yan, Y. Liu, L. Li, J. Wang, J. Mater. Chem. A 7 (2019) 15541–15563.
[11] S. Natarajan, Y.S. Lee, V. Aravindan, Chemistry–An Asian Journal 14 (2019) 936–951.
[12] M.L. Divya, S. Natarajan, Y.-S. Lee, V. Aravindan, J. Mater. Chem. A 8 (2020) 4950–4959.
[13] H. Zhang, M. Hu, Z.-H. Huang, F. Kang, R. Lv, Progress in Natural Science: Materials International 30 (2020) 13–19.
[14] H. Liu, X. Liu, H. Wang, Y. Zheng, H. Zhang, J. Shi, W. Liu, M. Huang, J. Kan, X. Zhao, D. Li, ACS Sustainable Chem. Eng. 7 (2019) 12188–12199.
[15] J. Yuan, X. Hu, Y. Liu, G. Zhong, B. Yu, Z. Wen, Chem. Commun. 56 (2020) 13933–13949.
[16] B. Li, J. Zheng, H. Zhang, L. Jin, D. Yang, H. Lv, C. Shen, A. Shellikeri, Y. Zheng, R. Gong, J.P. Zheng, C. Zhang, Adv. Mater. 30 (2018) 1705670.
[17] D. Majumdar, M. Mandal, S.K. Bhattacharya, Emergent Materials 3 (2020) 347–367.
[18] J. Asenbauer, T. Eisenmann, M. Kuenzel, A. Kazzazi, Z. Chen, D. Bresser, Sustainable Energy Fuels 4 (2020) 5387–5416.
[19] Z.-L. Xu, G. Yoon, K.-Y. Park, H. Park, O. Tamwattana, S. Joo Kim, W.M. Seong, K. Kang, Nature Communications 10 (2019) 2598.
[20] B. Jache, P. Adelhelm, Angew. Chem. Int. Ed. 53 (2014) 10169–10173.
[21] H. Kim, J. Hong, G. Yoon, H. Kim, K.-Y. Park, M.-S. Park, W.-S. Yoon, K. Kang, Energy Environ. Sci. 8 (2015) 2963–2969.
[22] M.L. Divya, S. Natarajan, Y.S. Lee, V. Aravindan, ChemSusChem 13 (2020) 5654–5663.
[23] J. Park, Z.-L. Xu, K. Kang, Front. Chem. 8 (2020) 432.
[24] K. Westman, R. Dugas, P. Jankowski, W. Wieczorek, G. Gachot, M. Morcrette, E. Irisarri, A. Ponrouch, M.R. Palacín, J.M. Tarascon, P. Johansson, ACS Applied Energy Materials 1 (2018) 2671–2680.
[25] P. Han, X. Han, J. Yao, L. Zhang, X. Cao, C. Huang, G. Cui, J. Power Sources 297 (2015) 457–463.
[26] B. Babu, P. Simon, A. Balducci, Adv. Energy Mater. 10 (2020) 2001128.
[27] J. Li, W. Zhang, X. Zhang, L. Huo, J. Liang, L. Wu, Y. Liu, J. Gao, H. Pang, H. Xue, J. Mater. Chem. A 8 (2020) 2463–2471.
[28] J. Zhu, Q. Zhang, H. Chen, R. Zhang, L. Liu, J. Yu, ACS Appl. Mater. Interfaces 12 (2020) 43634–43645.
[29] H. Wang, H. Niu, H. Wang, W. Wang, X. Jin, H. Wang, H. Zhou, T. Lin, J. Power Sources 482 (2021), 228986.
[30] Y. Wang, L. Zhang, H. Hou, W. Xu, G. Duan, S. He, K. Liu, S. Jiang, J. Mater. Sci. 56 (2021) 173–200.
[31] L. Yue, H. Zhao, Z. Wu, J. Liang, S. Lu, G. Chen, S. Gao, B. Zhong, X. Guo, X. Sun, J. Mater. Chem. A 8 (2020) 11493–11510.
[32] W. Li, M. Li, K.R. Adair, X. Sun, Y. Yu, J. Mater. Chem. A 5 (2017) 13882–13906.
[33] Y. Liu, J. Zhou, L. Chen, P. Zhang, W. Fu, H. Zhao, Y. Ma, X. Pan, Z. Zhang, W. Han, E. Xie, ACS Appl. Mater. Interfaces 7 (2015) 23515–23520.
[34] V. Aravindan, P. Sennu, Y.-S. Lee, S. Madhavi, The Journal of Physical Chemistry Letters 8 (2017) 4031–4037.
[35] S. Jayaraman, G. Singh, S. Madhavi, V. Aravindan, Carbon 134 (2018) 9–14.
[36] I. Cameán, A.B. García, I. Suelves, J.L. Pinilla, M.J. Lázaro, R. Moliner, J. Power Sources 198 (2012) 303–307.
[37] C. Ma, E. Cao, J. Li, Q. Fan, L. Wu, Y. Song, J. Shi, Electrochim. Acta 292 (2018) 364–373.
[38] P.T. Williams, Waste Manage. 33 (2013) 1714–1728.
[39] I. Hita, M. Arabiourrutia, M. Olazar, J. Bilbao, J.M. Arandes, P. Castaño, Renew. Sustain. Energy Rev. 56 (2016) 745–759.
[40] K. Januszewicz, P. Kazimierski, T. Suchocki, D. Kardaś, W. Lewandowski, E. Klugmann-Radziemska, J. Łuczak, Materials (Basel) 13 (2020).
[41] H. Wang, H. Yi, C. Zhu, X. Wang, H.J. Fan, Nano Energy 13 (2015) 658–669.
[42] B. Li, J. Guo, J. Huang, H. Xu, Z. Dong, X. Li, Materials 13 (2020) 1933.
[43] Z.Q. Li, C.J. Lu, Z.P. Xia, Y. Zhou, Z. Luo, Carbon 45 (2007) 1686–1695.
[44] A.C. Ferrari, J. Robertson, Physical Review B 61 (2000) 14095–14107.
[45] L. Bokobza, J.-L. Bruneel, M. Couzi, C 1 (2015).
[46] E.I. Bîru, H. Iovu, Raman spectroscopy 179 (2018).
[47] L.M. Malard, M.A. Pimenta, G. Dresselhaus, M.S. Dresselhaus, Phys. Rep. 473 (2009) 51–87.
[48] D.B. Schuepfer, F. Badaczewski, J.M. Guerra-Castro, D.M. Hofmann, C. Heiliger, B. Smarsly, P.J. Klar, Carbon 161 (2020) 359–372.
[49] R. Blume, D. Rosenthal, J.-P. Tessonnier, H. Li, A. Knop-Gericke, R. Schlögl, ChemCatChem 7 (2015) 2871.
[50] T. Susi, T. Pichler, P. Ayala, Beilstein J. Nanotechnol. 6 (2015) 177–192.
[51] R. Fu, X. Zhou, H. Fan, D. Blaisdell, A. Jagadale, X. Zhang, R. Xiong, Energies 10 (2017) 2174.
[52] M.W. Jessica Huesker, TobiasP Placke, Dilatrometric Study of the Electrochemical Intercalation of Bis(trifluoromethanee sulfonyl)imide and Hexafluorophosphate Anions into carbon -Based Positive Electrodes, 2015.
[53] F. Nacimiento, M. Cabello, G.F. Ortiz, R. Alcántara, P. Lavela, J.L. Tirado, Dalton Trans. 48 (2019) 5417–5424.
[54] Y. Jiang, J. Liu, energy & environmental materials 2 (2019) 30-37.
[55] J. Wang, J. Polleux, J. Lim, B. Dunn, The Journal of Physical Chemistry C 111 (2007) 14925–14931.
[56] V. Augustyn, J. Come, M.A. Lowe, J.W. Kim, P.-L. Taberna, S.H. Tolbert, H. D. Abruña, P. Simon, B. Dunn, Nat. Mater. 12 (2013) 518–522.
[57] G.G. Eshetu, G.A. Elia, M. Armand, M. Forsyth, S. Komaba, T. Rojo, S. Passerini, Adv. Energy Mater. 10 (2020) 2000093.
[58] Y.-S. Hu, Y. Lu, ACS Energy Lett. 5 (2020) 3633–3636.
[59] T.A. Pham, K.E. Kweon, A. Samanta, V. Lordi, J.E. Pask, The Journal of Physical Chemistry C 121 (2017) (1920) 21913–21922.
[60] T. Aida, K. Yamada, M. Morita, Electrochem. Solid-State Lett. 9 (2006) A534–A536.
[61] Y. Zhang, J. Jiang, Y. An, L. Wu, H. Dou, J. Zhang, Y. Zhang, S. Wu, M. Dong, X. Zhang, Z. Guo, ChemSusChem 13 (2020) 2522–2539.
[62] A.C.S. Jensen, H. Au, S. Gärtner, M.-M. Titirici, A.J. Drew, Batteries & Supercaps 3 (2020) 1306–1310.
[63] K. Kuratani, M. Yao, H. Senoh, N. Takeichi, T. Sakai, T. Kiyobayashi, Electrochim. Acta 76 (2012) 320–325.